Available online at www.sciencedirect.com
ScienceDirect
Journal of Marine Systems 66 (2007) 92–109
JOURNAL OF MARINE SYSTEMS
www.elsevier.com/locate/jmarsys

Air–sea gas exchange at extreme wind speeds measured by autonomous oceanographic floats

Eric D'Asaro [a,b,*], Craig McNeil [c]

[a] Applied Physics Laboratory, University of Washington, Seattle, WA 98105, USA
[b] School of Oceanography, University of Washington, Seattle, WA 98195, USA
[c] Graduate School of Oceanography, University of Rhode Island, Narragansett, RI 02882, USA

Received 16 March 2006; accepted 13 June 2006
Available online 27 October 2006

Abstract

Measurements of the air–sea fluxes of N_2 and O_2 were made in winds of 15–57 m s^{-1} beneath Hurricane Frances using two types of air-deployed neutrally buoyant and profiling underwater floats. Two "Lagrangian floats" measured O_2 and total gas tension (GT) in pre-storm and post-storm profiles and in the actively turbulent mixed layer during the storm. A single "EM-APEX float" profiled continuously from 30 to 200 m before, during and after the storm. All floats measured temperature and salinity. N_2 concentrations were computed from GT and O_2 after correcting for instrumental effects. Gas fluxes were computed by three methods. First, a one-dimensional mixed layer budget diagnosed the changes in mixed layer concentrations given the pre-storm profile and a time varying mixed layer depth. This model was calibrated using temperature and salinity data. The difference between the predicted mixed layer concentrations of O_2 and N_2 and those measured was attributed to air–sea gas fluxes F_{BO} and F_{BN}. Second, the covariance flux $F_{CO}(z)=\langle wO_2'\rangle(z)$ was computed, where w is the vertical motion of the water-following Lagrangian floats, O_2' is a high-pass filtered O_2 concentration and $\langle\rangle(z)$ is an average over covariance pairs as a function of depth. The profile $F_{CO}(z)$ was extrapolated to the surface to yield the surface O_2 flux $F_{CO}(0)$. Third, a deficit of O_2 was found in the upper few meters of the ocean at the height of the storm. A flux F_{SO}, moving O_2 out of the ocean, was calculated by dividing this deficit by the residence time of the water in this layer, inferred from the Lagrangian floats. The three methods gave generally consistent results. At the highest winds, gas transfer is dominated by bubbles created by surface wave breaking, injected into the ocean by large-scale turbulent eddies and dissolving near 10-m depth. This conclusion is supported by observations of fluxes into the ocean despite its supersaturation; by the molar flux ratio F_{BO}/F_{BN}, which is closer to that of air rather than that appropriate for Schmidt number scaling; by O_2 increases at about 10-m depth along the water trajectories accompanied by a reduction in void fraction as measured by conductivity; and from the profile of $F_{CO}(z)$, which peaks near 10 m instead of at the surface.

At the highest winds O_2 and N_2 are injected into the ocean by bubbles dissolving at depth. This, plus entrainment of gas-rich water from below, supersaturates the mixed layer causing gas to flux out of the near-surface ocean. A net influx of gas results from the balance of these two competing processes. At lower speeds, the total gas fluxes, F_{BO}, F_{BN} and $F_{CO}(0)$, are out of the ocean and downgradient.

1. Introduction

The greatest uncertainties in air–sea gas transfer rates and mechanisms are undoubtedly associated with high

* Corresponding author. Applied Physics Laboratory, University of Washington, Seattle, WA 98105, USA.
E-mail address: dasaro@apl.washington.edu (E. D'Asaro).

0924-7963/$ - see front matter © 2006 Elsevier B.V. All rights reserved.
doi:10.1016/j.jmarsys.2006.06.007

wind speeds (U_{10}). Prior field studies have been limited to $U_{10}<22$ m s^{-1} (Watson et al., 1991; Farmer et al., 1993; Nightingale et al., 2000). At high winds, bubbles are believed to play an increasingly important role in gas transfer. Bubble clouds increase the effective ocean surface area available for gas transfer and thus increase air–sea gas fluxes. Prior observations have showed that bubbles can be carried by downward-going currents caused by turbulent eddies, Langmuir circulations and/or wave breaking to depths where they either partially or fully dissolve (Farmer et al., 1993). In this case, gas transfer occurs at pressures higher than atmospheric thereby allowing gas to be injected into the ocean even when the ocean is supersaturated. Theoretical studies (Woolf and Thorpe, 1991; Keeling, 1993; Woolf, 1997) support this prediction. Two fundamental questions that limit a comprehensive understanding of air–sea gas transfer over the natural range of winds speeds are: (1) what process limits gas transfer rates at extreme wind speeds, and (2) what are the associated maximum transfer rates?

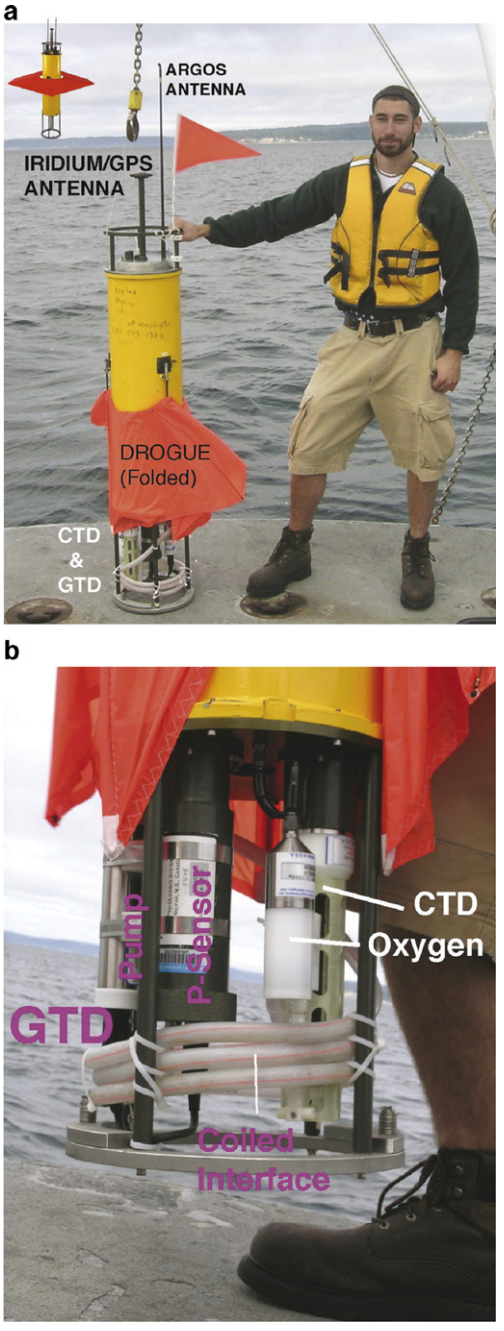

Fig. 1. The Lagrangian float. (a) Drogue folded for deployment or profiling. Float configuration with drogue open, as during its Lagrangian drift, is shown in upper left. (b) Sensor details.

These questions need to be answered to reduce uncertainty in the net global air–sea flux of CO_2. Direct estimates of the net uptake rate of atmospheric CO_2 by the oceans are based on regional and seasonal interpolation of measurement-based estimates of the air–sea CO_2 partial pressure difference (Δp) and wind speed (U_{10}). The flux (F) is estimated using parameterizations of the form:

$$F = K_T(S_c/660)^{-\frac{1}{2}} S\Delta p \qquad K_T = aU_{10}^N \tag{1}$$

where K_T is the gas transfer velocity, S is the seawater solubility, $S_c = \nu/D$ is the Schmidt number (660 for CO_2 at 20 °C) with ν the kinematic viscosity of water, D the molecular diffusivity of the gas, and a and N constants (Liss and Slater, 1974). This form for F is based on the physics of diffusion-limited gas transfer across a turbulent and wavy sea surface. The form for K_T is empirical (Liss and Merlivat, 1986; Wanninkhof, 1992; Wannikhof and McGillis, 1999; Nightingale et al., 2000) with effective values of N varying from 1 to 3. Uncertainty in N leads to an uncertainty in the estimates of the net global CO_2 uptake by the oceans by 70% (Takahashi et al., 2002). If hurricanes are also included, even greater uncertainties are predicted (Bates et al., 1998; Bates, 2002). This paper describes measurements of the processes of gas transfer at extreme high winds and the associated transfer rates. McNeil and D'Asaro (2007-this issue) describe modeling and parameterization of the observations reported here.

2. Instrumentation

2.1. Lagrangian floats

2.1.1. Mission

Two Lagrangian floats (Fig. 1) were deployed ahead of Hurricane Frances by the 53rd 'Hurricane Hunter'

squadron of the U.S. Air Force Reserve on 31 August 2004 near 22.15°N, 69.8°W. Accurate forecasts and targeting placed these floats so that they experienced nearly the maximum winds of the storm (Figs. 2 and 3).

Each float executed a complex mission. The float was contained in an air deployment package for launch. A parachute slowed its descent to the ocean surface. Dissolving salt blocks released the strapping of the deployment package allowing the float to sink. It awakened at 2-m depth and immediately surfaced to get a GPS fix, then slowly profiled to 120 m, stopping at selected isopycnals (Fig. 2b). Float 21 suffered a software malfunction during the downward profile causing it to surface briefly, but it recovered and continued its mission. The floats then profiled to the surface to obtain a second GPS fix as the hurricane arrived. During the storm the floats adjusted their density to match that of the 10–25-m water. They were repeatedly carried across a 40-m deep mixing layer by turbulent eddies (red and blue trajectories in Fig. 2b). These vertical motions were not due to active float control, but instead followed the water's motion. After the hurricane passed, the floats surfaced, obtained a GPS position, and then performed a second low speed actively-controlled profile to 120 m. At the end of the mission, the floats surfaced and data were retrieved via the Iridium global satellite system. A research vessel recovered the floats on 2 October 2004.

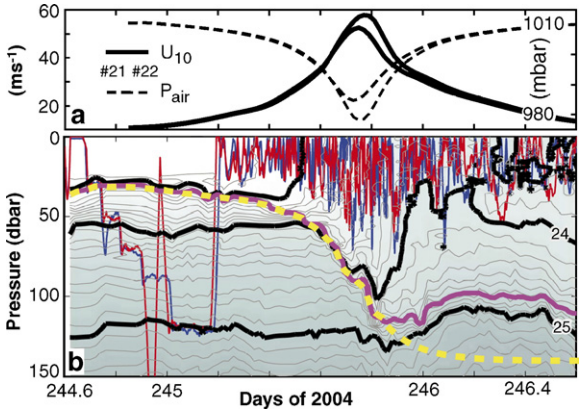

Fig. 2. Meteorological and oceanographic environment during the passage of Hurricane Frances at the float locations. (a) Atmosphere: Wind speed at 10 m height (U_{10}) and atmospheric pressure (P_{air}) versus time at floats 21 (red) and 22 (blue). (b) Ocean: Depth–time evolution of potential density (σ_θ, grey/black contours), depth of floats 21 (red) and 22 (blue), and mixing layer depth H estimated from the data (magenta) and used in the mixing model (yellow). (For interpretation of the references to colour in this figure legend, the reader is referred to the web version of this article.)

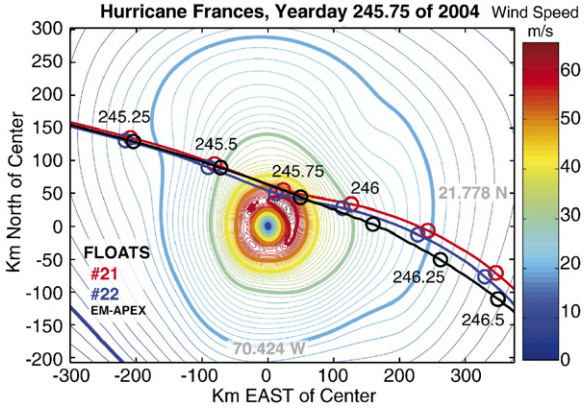

Fig. 3. Hurricane Frances wind map. Wind speed map for Hurricane Frances from day 245 18Z H*WIND analysis. Wind speed is indicated by colored contours with a solid contour every 10 m s^{-1}. Trajectories (eastward going) of the floats in the coordinate system of the (westward going) storm are shown. (For interpretation of the references to colour in this figure legend, the reader is referred to the web version of this article.)

2.1.2. Float design and operation

The float displaces about 50 L and is about 1.4 m long. It is designed to follow the three-dimensional motion of the surrounding water by adjusting its density to match and through the drag of a cloth drogue (area of 1 m^2). Each float measured temperature, salinity, pressure, dissolved O_2 and total gas tension at 15 and 30-s intervals during profiling and the Lagrangian drift periods, respectively. Accurate ballasting was achieved through an understanding of the float's equation of state, i.e., its mass, volume, and thermal expansion and compressibility (D'Asaro, 2003a). The mass of the float was measured; expansion coefficients were measured in a laboratory tank, in specially designed test missions, or estimated based on material properties. Volume was computed by equilibrating the float at selected isopycnals on the initial profile in water, computing the water's density from the measured temperature and salinity, thereby computing the float's density. During the Lagrangian drift, the float's density was adjusted to match that of the water. Adjustments were only made in a depth range of 10–25 m to eliminate errors caused by bubble contamination of the CTD near the surface and to match the float's density just to that of the mixed layer so that it would return to the mixed layer if advected downward into the underlying stratification. An upward bias of about 1 g was applied to the computed float buoyancy in order to compensate for possible errors in the ballasting calculations. We estimate that the residual buoyancy in the mixed layer is only a few grams in mid-mixed layer, resulting in a motion relative to the water of a few millimeters per second, significantly

smaller than the many centimeters per second of vertical water motion. The buoyancy may be larger near the surface, either positive, due to bubbles attached to the float, or negative due to the reduced density of the water due to such bubbles. Dynamical estimates of errors caused by such effects are discussed in Section 4.1 below.

The float's measured depth, inferred from pressure, is nearly insensitive to the vertical displacements of surface waves. The float's pressure sensor therefore measures the true depth below the surface. This is because Lagrangian particles moving under the influence of linear surface waves follow surfaces of constant pressure (D'Asaro et al., 1996). This is most easily seen by noting that a particle floating at the ocean surface is both Lagrangian and at a surface of constant pressure. An ideal Lagrangian float therefore measures no pressure fluctuations resulting from linear surface waves. Small deviations from this ideal behavior result from the float's pressure sensor not exactly following a Lagrangian trajectory even if the float does. There is also no guarantee that this will be true for nonlinear surface waves. Nevertheless, we see little evidence for surface waves in our measured pressure, despite the very large (10 m significant wave height; Black et al., in press) surface waves during Hurricane Frances.

2.2. EM-APEX float

The Electromagnetic Autonomous Profiling Explorer measures temperature, salinity and velocity every 5 m during vertical profiles moving at 0.12 m s^{-1}. A single EM-APEX float was air-deployed with the two Lagrangian floats. Two others were deployed elsewhere ahead of Hurricane Frances. The EM-APEX is a standard Webb Research APEX profiling float with an APL-UW subsystem for measuring electric fields induced by the ocean currents moving through the vertical component of the Earth's magnetic field (Sanford et al., 1978). These measurements were used to calculate profiles of horizontal ocean current with an unknown offset. The *T* and *S* measurements are obtained from the Sea Bird Electronics SBE-41 CTD, the same sensor used on the Lagrangian floats. Electrodes on a right cylindrical shell surrounding the lower half of the float sense the motionally induced voltages. The voltages are amplified, digitized, processed into horizontal velocity components and stored within the float. Other measurements are magnetic compass and instrument tilt.

The float was deployed using the same air package as the Lagrangian floats. For the first 10 h it profiled from the surface to 200 m. For the next 5 days, it profiled from 30 m to 200 m and back every 4000 s with excursions to 500 m every 16 h (i.e., half an inertial period). The float position was determined by the GPS system whenever it surfaced. The *T*, *S*, *V*, position and engineering data were processed within the float and transmitted over the Iridium global cell phone system at the end of the 5-day submersion mission and half inertial period profiles until recovery. A depth–time map of potential density, computed by combining data from all three floats, but mostly determined by the EM-APEX data, is shown in Fig. 2b.

2.3. Navigation

GPS fixes and velocity data from the EM-APEX were used to compute the positions of all three floats. All three floats obtained pre-storm and post-storm GPS positions. Interpolation between these fixes was done using velocity data from the EM-APEX float. The velocity profiles from the EM-APEX were interpolated to the depths and times of each float and integrated in time from the pre-storm fix. An offset velocity was added to adjust the computed post-storm position to match the GPS fix. The net effect of this offset was about 5 km for the Lagrangian floats.

2.4. Winds and air pressure

Winds and atmospheric pressure were estimated using the H*WINDS analysis system (Powell et al., 1998). Wind data from aircraft microwave wind sensors (Uhlhorn and Black, 2003), air-deployed dropsondes and QUICKSCAT satellite winds were combined in a storm-centered coordinate system. Analyses were done centered at 18Z on days 243–247. The bulk of the data in each analysis came from a single survey by a NOAA-P3 aircraft. The results of this paper rely primarily on the analysis, and associated flight on day 245, when the storm was over the float array. This unpublished data was obtained and made available by the Hurricane Research Division of NOAA. Fig. 3 shows the wind speed from the day 245 18Z analysis and the positions of the three floats relative to the storm center as the westward moving storm passed over them. Winds at the floats were computed at each time in the float time series by first interpolating the analyzed wind fields to the float position in a storm centered coordinate system. Winds computed from the two wind fields closest in time were then interpolated in time.

The estimated wind fields contain errors. The aircraft winds were taken along 8 radial lines from days 245.7 to 245.85, close to the time of maximum winds at the floats. However, only two lines occupied the same storm

quadrant as the floats; none was closer than 50 km to the floats. The storm was moving at about 5 m s^{-1} so an interpolation over 50 km is equivalent to interpolation over about 10^4 s. During this period, satellite images show that Frances was undergoing an eyewall replacement cycle during which a small intense eye was replaced by a larger eye. The net effect of the eye replacement can be seen by comparing the 245.75 wind field to the 246.75 field along a line 52 km north of the storm center and parallel to its track, the approximate float track relative to the storm. Peak winds drop from 55 m s^{-1} to 45 m s^{-1}, but the width of the region with greater than 30 m s^{-1} winds increases from 360 km to 550 km. In Fig. 2a, this change can be seen as the asymmetry between the more rapid rise of the wind, when the eye is smaller, and its slower fall when the eye is larger. In reality, however, this change may happen much more rapidly than assumed in our analysis and may be accompanied by significant asymmetries in the wind fields. A rapid switch from a small intense wind pattern to a broader weaker one could shift the time of maximum wind forward in time relative to what is seen in our analysis.

Atmospheric pressure was computed from the day 245 18Z wind field using the gradient wind balance applied to the radially averaged wind field in the NE quadrant of the storm. The resulting pressure gradient was radially integrated to obtain a pressure distribution as a function of radius. Pressures at 10 m height were obtained from GPS dropsondes deployed by the NOAA aircraft. The level of the computed pressure was adjusted to match the mean of the dropsonde pressure for radii greater than 75 km. Fig. 4 compares the dropsonde and gradient winds. Outside of 25 km radius they agree to within a few millibars. Near the hurricane's eye a correction is needed, but this does not affect the results presented here.

2.5. O_2 sensor and calibration

Each Lagrangian float carried a Seabird Electronics SBE-43 O_2 sensor integrated into the SBE-41 CT (conductivity/temperature) sensor. Both O_2 sensors were calibrated three times each in June and July 2004 at Seabird Electronics, the last time on 19–20 July. The calibrations agreed to better than 1 μmol kg^{-1} for both the same sensor and between sensors. Float 22 was calibrated against water samples taken within 1 m of the float sensor during Puget Sound testing on 15 July. The agreement was better than 1 μmol kg^{-1}.

Both sensors were similarly calibrated after the cruise on November 16–17, 2004 at Seabird. The November calibrations are 2.4% or 6 μmol kg^{-1} lower than the July values, consistent with the known linear drift of these sensors when stored or operated in the presence of oxygen (Nordeen Larson, personal communication, 2005).

During the deployment, however, and immediately upon recovery (2 October 2004) in a pumped, circulating bath on the ship, the two O_2 sensors differed consistently by 4 μmol kg^{-1} with no evidence for a dependence of this difference on depth or time. There is no definitive explanation for this difference, although changes of this magnitude can occur due to sensor drift, fouling or other problems. Float 21's calibration was set by assuming a drift linear in time between the pre-cruise and post-cruise calibrations, i.e., 42 out of 119 days, 35% of the way from the pre-cruise to post-cruise calibrations. Float 22's calibration was set to minimize the difference in the resulting pre-storm oxygen profile with Float 21 by using an 85% mix of the pre- and post-cruise calibrations. This is subjective but yields pre-storm oxygen supersaturations, computed using the Garcia and Gordon (1992) equations, within the range of historical values and keeps both calibrations between the pre- and post-cruise values. The NOAA ocean atlas (Conkright et al., 2002) shows 3–5% supersaturation; our own analysis of all available NODC profiles from this region always shows some supersaturation. Assuming that the true calibration lies somewhere between the pre- and post-cruise values, the absolute uncertainty in calibration is 3 μmol kg^{-1}. Differences between the two sensors during the measurements due to calibration errors are less than 1 μmol kg^{-1}.

2.6. Gas Tension Device (GTD)

Gas tension, defined as the sum of all dissolved gas partial pressures, was measured by a GTD that operates by equilibrating a sample volume of gases with seawater

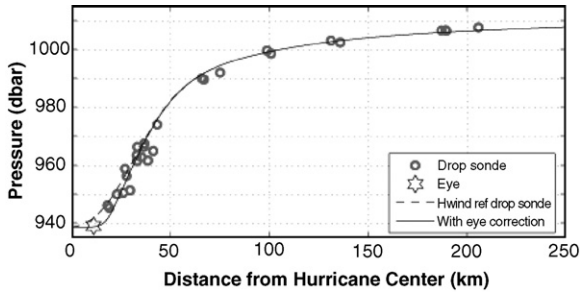

Fig. 4. Air pressure analysis. Pressure field computed from Fig. 3 using the gradient wind balance (dashed line) and adjusted (solid line) to fit aircraft dropsonde observations (circles).

through a gas permeable polydimethyl-siloxane (PDMS) membrane. It senses the pressure in this volume with a Paroscientific model 230A barometer. A novel 3-m-long tubular shaped membrane interface was employed to achieve a large surface area of membrane and a short equilibration time. The membrane interface was contained in a coiled tube through which seawater was pumped at approximately 6 L min^{-1} using a Sea-Bird Electronics model 5T pump running at 6 W. Absolute uncertainty in pressure sensor calibration is ±1.0 mbar for Float 21 and ±0.1 mbar for Float 22 based on analysis of pre- and post-deployment calibrations (Table 1).

The new gas tension device used here has a large hydrostatic response associated with compression and decompression of the membrane (McNeil et al., in press), which is apparent as a large increase in measured gas tension as the float descends from the surface (Fig. 5). Accordingly, raw GTD data does not accurately reflect gas tension on short time scales if pressure is also changing. Two techniques were used to overcome this. During the pre- and post-storm profiles, the float rested at selected isopycnals, thereby allowing time for the GTD to equilibrate. These measurements can be interpreted unambiguously as gas tension. During the Lagrangian drift, the dynamical model of McNeil et al. (in press) was used. It models the GTD response using a equilibration time and bulk modulus of the membrane that with pressure thereby removing most of the pressure effects. Remaining noise was minimized using a low pass filter with an averaging time of about 7000 s. Comparison with the pre- and post-storm profiles showed that the remaining signal had a residual pressure dependence of 0.1 and 0.15 μmol kg^{-1} db^{-1} for floats 21 and 22, respectively, due to imperfections in the model coefficients. This residual was removed from the data. N_2 concentrations were then computed from gas tension, O_2 concentration, T and S following McNeil et al. (2006) and using the saturation equations from Hamme and Emerson (2004); this procedure assumes that Ar was saturated to the same level as N_2.

Table 1
Calibrations for the GTD used in the Puget Sound and Hurricane Frances experiments

Experiments	Puget Sound, July 7–17, 2004		Hurricane Frances, September 2004	
Float #	#21	#22	#21	#22
GTD	SN 24-035-43	SN 24-034-43	SN 24-035-43	SN 24-034-43
Pressure sensor	SN 89678	SN 90125	SN 89678	SN 90125
Range	0 – 6890 mbar	0 – 2070 mbar	0 – 6890 mbar	0 – 2070 mbar
Calibrations	±0.1 mbar	±0.1 mbar	±1 mbar	±0.1 mbar
Maximum drift	<1.4 mbar/week	None	<0.14 mbar/week	None
Time between calibrations	3 days	3 days	95 days	95 days

For the Hurricane Frances experiment, pre-deployment GTD calibrations were performed at APL-UW on 17 July 2004 and post-deployment GTD calibrations were performed at WHOI on 18 October 2004.

2.7. Sensor performance in a bubbly ocean

A unique aspect of these data is the strong role for bubbles in gas exchange. A simple calculation suggests that the gas sensors will not be significantly biased by the presence of bubbles. We assume that because both sensors are strongly pumped, bubbles do not concentrate within the plumbing and the bubble concentrations at the sensing membranes are the same as in the seawater. We show below that the maximum void fraction of bubbles is about 10^{-3}. We assume that the dissolved gas sensors measure the time-averaged partial pressures of the gases in the seawater and the bubbles, proportioned by the ratio of their volumes. Near the sea surface, we assume that the partial pressures of the gases in the bubbles differ from the oceanic levels by no more than 10%. The equilibrated dissolved gas sensors will therefore differ from actual oceanic gas levels by no more than 0.01%. At 10-m depth, hydrostatic pressure will compress the bubbles such that the gases in the bubbles will have partial pressures approximately 100% higher than oceanic levels. The equilibrated dissolved gas sensors will therefore read slightly higher than the actual oceanic gas levels, but no more than approximately 0.1% for each gas. Alternatively, assuming that because the dissolved gas sensors use a flat membrane, the contribution of the bubbles should be weighted by their area rather than their volume. In this case, the equivalent void fraction is about 10^{-2} and the resulting error in gas measurements associated with bubbles hitting the membrane is 0.1% and 1%, respectively. In either case, the effect is negligible for the SBE-43 and GTD.

3. Air–sea fluxes from budgets

3.1. Approach

The measurements of temperature and salinity were used to formulate a model of the upper ocean mixing during the storm. This is possible because the very small role that air–sea heat flux plays in changing the upper ocean temperature profile makes temperature changes dependent almost entirely on mixing. Furthermore, the

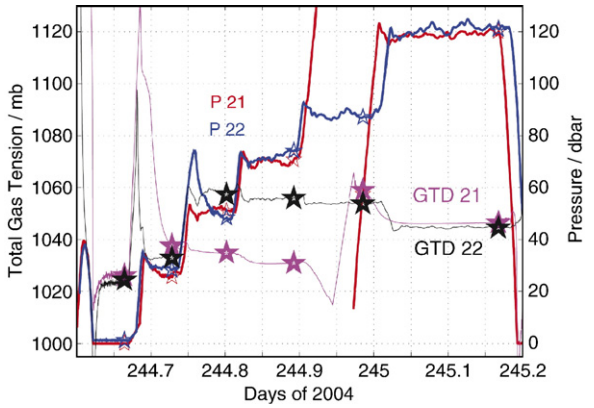

Fig. 5. Gas tension on initial profile. Raw pressure and gas tension data for float 21 (red/magenta) and float 22 (blue/black) during the pre-storm profile. The large transients associated with GTD adjustment are evident during times of changing pressure. The stars indicate times when GTD was well equilibrated; these points were used to create the pre-storm profile. The GTD on float 21 was blocked by water drops from about days 244.75 to 244.92. These two (magenta) data were therefore not used. The large pressure excursion of float 21 starting at day 244.9 was the result of a software malfunction from which the float successfully recovered. The data point at day 244.98 for float 21 was therefore also not used. (For interpretation of the references to colour in this figure legend, the reader is referred to the web version of this article.)

very strong mixing makes a simple depth–time model effective for much of the storm. This model is then used to remove the effects of mixing from the measured gas concentrations and thereby estimate the air–sea fluxes as a residual.

3.2. Temperature and salinity evolution

The density structure (Fig. 2b) shows the dominant role of vertical mixing in changing the near-surface properties. A surface layer with weak density stratification is always present. The layer depth increases from 25 m before the storm to 120 m after its passage. This deepening mixes roughly 100 m of water into the mixed layer across its bottom boundary leading to an approximately 2 °C cooling of the mixed layer. Surprisingly, the floats do not transit this entire layer, but remain in the well-mixed upper 20–50 m. The lower part of the layer is weakly stratified. Velocity measurements from the EM-APEX reveal that this lower layer remains close to a critical Richardson number, implying that mixing in this region is a result of shear instability rather than direct surface forcing.

The boundary layer can be divided into several distinct regimes. A rapidly mixed wave-boundary layer in which wave breaking plays a major role in mixing extends to a maximum of 10-m depth. Observations reveal a high concentration of bubbles in this region; these play a large role in gas-transfer at high wind speed and may also play a role in controlling the water density. Below this is a nearly-uniform turbulent boundary layer, extending to no more than 60 m deep, mixed by eddies driven by surface wind and waves. The float trajectories show that these eddies extend all the way across the layer. The next layer is also turbulent, but driven by wind-forced shear forcing a critical Richardson number. The turbulent eddies are smaller than the layer thickness, resulting in true diffusive mixing. Temperature and salinity have weak gradients here. The bottom of the boundary layer is marked by a roughly 10-m thick step in density, underlaid by a nearly laminar ocean interior. Details of this multi-layered structure will be the subject of a later manuscript.

Despite these differences in dynamics, it appears that temperature, salinity and gasses are mixed through all three turbulent layers fast enough that the concept of a well-mixed layer extending to a "mixed layer depth" H is useful. This simple approach is therefore used for the rest of the analysis.

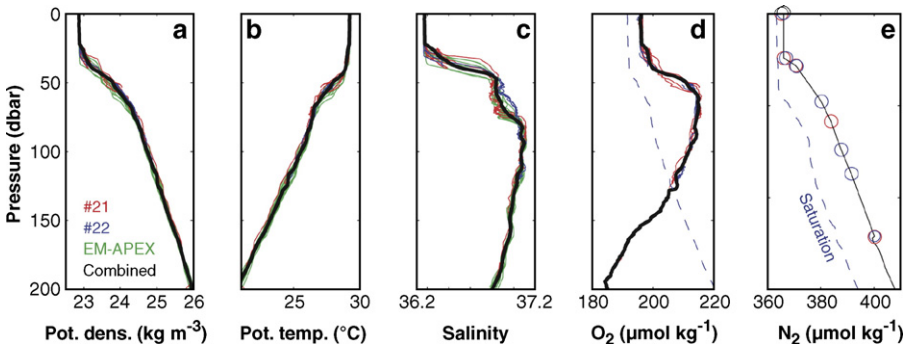

Fig. 6. Pre-storm profiles. Each panel shows the data from all three floats (color coded) and the combined profile (black) used in the analysis. (a) Potential density; (b) potential temperature; (c) salinity; (d) dissolved O_2 concentration; (e) dissolved N_2 concentration. The N_2 profile is extended below the deepest data assuming a constant supersaturation. Blue dashed curve is 100% saturation for each gas. (For interpretation of the references to colour in this figure legend, the reader is referred to the web version of this article.)

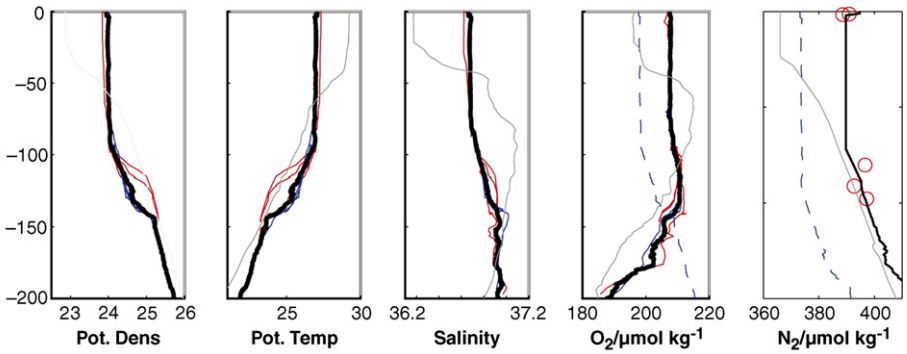

Fig. 7. Post storm profiles as in Fig. 6. Light grey lines show pre-storm profiles.

3.3. Pre- and post-storm profiles

Figs. 6 and 7 show the profiles of all variables before and after the storm, respectively. These were constructed using data from all three floats, when available, with the colors indicating the float. The combined profile (black) was computed from the average of these. The pre-storm profiles are highly consistent, because the three floats were no more than a few kilometers apart. The post-storm profiles, which are not used quantitatively in the analysis, show considerable differences, reflecting the separation of float 21 by about 24 km from the other two floats. Comparison of the pre- and post-storm profiles clearly show the deepening of the mixed layer.

3.4. Mixing model

The rate of entrainment into the mixed layer from below is estimated based on a time series of mixing depth $H(t)$ and the pre-storm profile of each variable. Fig. 8 shows the model geometry labeled for potential temperature θ with initial profile $\theta(z)$ and a temperature step $\Delta\theta$ across the bottom of the mixed layer. A mixed layer of depth H is assumed with temperature θ_m. It is cooled from below by entrainment and from above by a heat flux F_θ. For $F_\theta=0$, heat conservation requires

$$\theta_{m0} = \frac{1}{H}\int_{-H}^{0} \theta_0(z)\mathrm{d}z. \quad (2)$$

In general

$$\theta_m = \theta_{m0} - \int_0^t F_\theta \mathrm{d}t. \quad (3)$$

Inverting Eq. (3) to estimate the surface flux yields

$$F_\theta = \frac{\mathrm{d}}{\mathrm{d}t}[(\theta_m - \theta_{m0})H] \quad (4)$$

with units of °C m s^{-1}. This will be expressed as W m^{-2} s^{-1} after multiplying by ρC_v the specific heat per unit volume. For gases, Eqs. (2), (3) and (4) are used with the gas concentration, μmol kg^{-1}, used in place of θ to yield a surface gas flux, μmol kg^{-1} m s^{-1}, that will be expressed as μmol m^{-2} s^{-1} after multiplying by the water density ρ.

3.5. Mixed layer depth

The mixing model described above assumes that vertical mixing is the only important process. The 0–200-m ocean heat content, computed from the temperature equivalent of Fig. 2b, is nearly constant from before the storm through day $t_0=245.85$, thereby justifying the use of a one-dimensional model during this time. An initial time series of mixing depth H_0 was obtained by hand digitizing the depth of maximum stratification at the bottom of the mixed layer (solid magenta line in Fig. 2b). For times less than t_0, $H=H_0-12$ m was used with the offset chosen so that the mixing model best matched the initial mixed layer properties. The time series of H was further smoothed with a 4-h running mean. For times greater than t_0, the heat content of the upper ocean changes by much more than can be attributed to air–sea heat fluxes. Modeling studies of this storm (James Price, personal communication, 2005) indicate that this is because both vertical and horizontal heat advection become important. Although vertical mixing still controls the mixed layer properties, changes in the depth of the mixed layer no longer accurately reflect the amount of mixing. The same mixing model was used, but with H set to best match the mixed layer properties: $H=H_0+H_1(1-e^{-(t-t_0)/T_H})$ with H_1 and T_H chosen to provide a good fit with the temperature data. This estimate of mixed layer depth is shown as the yellow dashed line in Fig. 2b.

3.6. Air–sea heat flux

The air–sea heat flux at the floats is used to correct the temperature mixing model using Eq. (3). It was computed using standard bulk formulae (Cione et al., 2000). Continuous measurements of air–sea temperature difference and near-surface humidity were estimated from two different averaged profiles of these quantities as a function of radius. First, the estimates from historical data (Cione et al., 2000) were used. For radii of 0°, 0.375°, 1.12°, 1.875°, 2.875°, 4.25° and 1000° (i.e., infinity) (1° = 111.2 km) the relative humidity was taken as 97%, 96.4%, 91.3%, 82.1%, 87.9%, 85.4% and 85%, respectively. Similarly, for radii of 0°, 1.4°, 2.2°, 2.7°, 3.3°, 4° and 1000° the air–sea temperature difference was taken as 2.5°, 2.3°, 0.8°, 0.1°, 0.4° and 0°, respectively. Data were interpolated from these tables to other radii. Second, the dropsondes taken on day 245 in Hurricane Frances were averaged to construct a similar table with radii of 0, 200 and 1000 km, respective relative humidities of 98%, 70% and 95% and air temperatures of 25°, 27.5° and 28°. Air–sea temperature differences were computed from these and the observed mixed layer temperature at each float. Standard bulk formulae were used with exchange coefficients for sensible heat of 1×10^{-3} and latent heat of 1.2×10^{-3}.

The resulting heat fluxes at the height of the storm are roughly -400 W m^{-2} using the first model and roughly -600 W m^{-2} using the second, with the latent heat dominating. These fluxes act to cool the ocean and supply enthalpy to the hurricane. The total heat change due to air–sea flux is 3.9×10^{7} and 6.3×10^{7} J m^{-2} for the two methods, respectively. The average of the two methods is used in the analysis. Note that the air–sea heat flux accounts for only a few percent of the mixed layer temperature change. Its exact specification is not important because the changes in mixed layer temperature are almost entirely controlled by downward flux of heat caused by the growth of the warmer mixed layer downward into the colder thermocline.

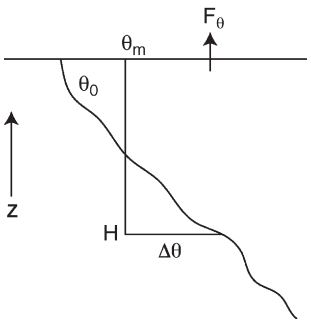

Fig. 8. Sketch of mixing model.

3.7. Testing the mixing model against temperature data

Fig. 9a tests the mixing model against the mixed layer temperature data. The red and blue lines show the mixed layer temperature from the two Lagrangian floats; the green line is their average, which is used for model comparison. The dashed magenta line is the prediction of Eq. (2), i.e., mixing alone. It lies slightly above the data. The solid magenta line is the prediction of Eq. (3), i.e., mixing plus surface heat flux. It fits the data very well. This demonstrates that the model, with some minor tuning of the mixed layer depth, can accurately predict the mixed layer temperature.

3.8. Salt flux

The salinity S budget provides an additional check on the model accuracy. The net surface freshwater flux is computed from $F_R = H/S\mathrm{d}(S-S_m)/\mathrm{d}t$. The total implied freshwater change, about 0.3 m, is qualitatively consistent with net rain rates in hurricanes, but otherwise provides little quantitative guidance on model accuracy.

3.9. Bulk gas fluxes

The mixing model is used to compute air–sea fluxes of O_2 and N_2 (Fig. 9c–f). The concentrations of both gases increase with depth in the upper 100 m (Fig. 9c–e). Vertical mixing during the storm therefore acts to increase their mixed layer concentrations with time. The mixing model predicts (Fig. 9d and f, magenta dashed lines) an increase of 15 μmol kg^{-1} for N_2 and 13 μmol kg^{-1} for O_2. The observed increases (Fig. 9d and f, green lines) are even larger, 30 μmol kg^{-1} for N_2 and 15 μmol kg^{-1} for O_2. Following (4), we interpret the difference between the modeled gas concentration C_m and observed concentration C as due to net air–sea flux of gas, $F_{BC} = \frac{\mathrm{d}}{\mathrm{d}t}[H(C-C_m)]$. These 'bulk' fluxes for O_2 (F_{BO}) and N_2 (F_{BN}) are shown in Fig. 10a and b. We use the convention that gas flux into the ocean is positive. Two estimates of the bulk fluxes, 'fast' and 'slow', are shown with different time smoothing. The red curves are computed after additionally smoothing C and C_m using a third order Butterworth filter with an averaging time of about 0.2 day.

Errors in the bulk flux estimates result from several sources, and their contributions are not easy to quantify. First, as the floats move apart, differences between the gas measured at the two floats increase to about 25% of the

average by day 245.9 for both O_2 and N_2. This introduces an uncertainty of about 25% in the value of the peak fluxes. After day 245.9 the difference between the two floats remains constant or decreases slightly and this effect should not cause additional errors.

Second, the mixing model becomes increasingly artificial after day 245.9 as horizontal effects become important. The use of an artificial mixed layer depth does appear to accurately reproduce the mixed layer temperature, but this does not necessarily mean that this artifice will accurately model all aspects of the gas budgets. At a minimum, the fluxes are uncertain to the fractional difference between the true mixed layer depth and the one used in the model. This increases rapidly from a few percent at day 245.8, to almost 30% by day 246.

Third, it is clear that smoothing is necessary to compute meaningful fluxes, particularly for N_2. After day 246 the 'slow' data (blue in Fig. 10a and b), which is more heavily filtered, have lower errors than the 'fast' data (red). We assume that the supersaturation of the ocean ensures that gas fluxed out of the ocean at all times during this period and note that the 'fast' flux estimates reach zero once or twice. The 'slow' smoothing time is about 0.08 day, so there are about 9 independent estimates. This is roughly consistent with a standard deviation equal to the mean, or 100% error. The additional 'slow' smoothing increases the effective smoothing time to about 0.2 day, a factor of 2.5, which should decrease the standard error to 63%, which we take as an our estimate for the 'slow' data after day 246. Visually, the additional smoothing seems more effective than this in reducing the noise, perhaps because the spectra are red, rather than white.

We estimate the peak fluxes using the 'fast' fluxes. These are subject to the first error, as the floats are separating most rapidly at this time. Their error is therefore estimated at 25%; reasonable confidence limits might be twice that. This is consistent with Fig. 9, which clearly shows gas fluxing into the ocean during this period. We estimate the post-peak fluxes using the 'slow' fluxes. These are subject to the second and third errors, with the third dominating. Their error is estimated at 60%, consistent with the interpretation that we know the sign of these fluxes, clearly out of the ocean, but that their magnitude has a large error.

The transition from gas influx to efflux near day 256.8 is problematic for this analysis. The 'fast' and 'slow' fluxes behave quite differently for O_2 here and it is not obvious what time averaging should be used. Accordingly, estimates of gas flux ratio (Fig. 10c) have large errors. The winds are still quite high, but with a large uncertainty

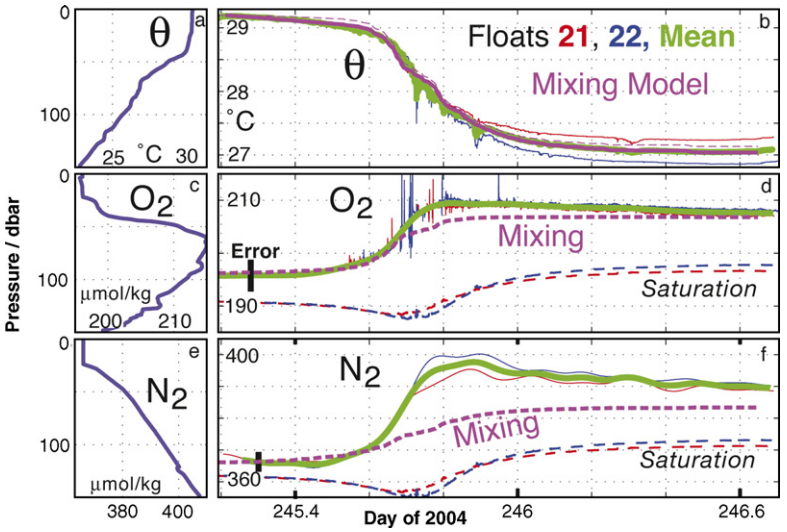

Fig. 9. Evolution and modeling of mixed layer temperature and dissolved gas concentrations. Left column, panels a, c, e: Pre-storm profiles of potential temperature (q), O_2 and N_2 concentration. Right column, panels b, d, f: Mixed layer values of these quantities at floats 21 (red) and 22 (blue) and the average of these two values (green) and additionally smoothed (in panels d and f) by applying a low pass filter (period of 10,000 s). Model mixed layer values (magenta dashed) are computed by mixing the pre-storm profiles in panels a, c and e to depth H (see Fig. 2b). A model mixed layer temperature that also includes the effect of surface heat flux is shown in panel b (magenta solid). Air–sea gas fluxes, i.e., F_{BO} and F_{BN}, are calculated from the difference between the model (magenta) and observed (green) mixed layer gas concentrations. The mixed layer dissolved gas saturation levels with respect to local atmospheric pressure at each float (red/blue dashed) and the estimated uncertainty associated with sensor calibration and data processing (black bars) are shown in panels d and f. (For interpretation of the references to colour in this figure legend, the reader is referred to the web version of this article.)

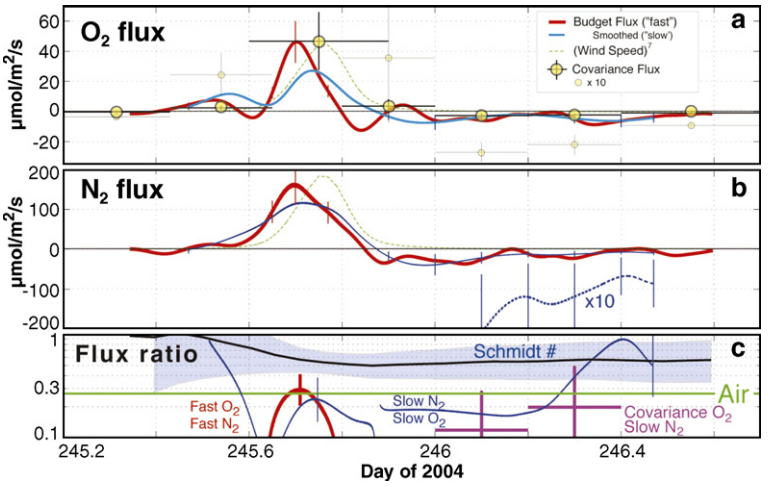

Fig. 10. Air–sea gas flux measurements. (a) O_2 flux F_{BO} (red) derived from mixed layer O_2 budget ("fast") and with additional smoothing (green, "slow"). Covariance O_2 flux F_{CO} (yellow circles) with lines showing temporal averaging and one standard deviation errors. F_{CO} multiplied by 10 (small yellow circles). (Wind speed)^7 with arbitrary scale (green dashed). (b) Same, but for F_{BN} the N_2 budget-derived flux. Selected values are multiplied by 10 for clarity. (c) Ratio of O_2 flux to N_2 flux ($R_{NO}=F_{BO}/F_{BN}$) computed from ratio of slow fluxes near peak of storm (red) and fast fluxes (blue) and using covariance flux (F_{CO}/F_{BN}, purple). Model R_{NO} assuming (1) (black) and complete bubble dissolution (purple, "Air"). Shading shows errors due to gas sensor calibration uncertainties. (For interpretation of the references to colour in this figure legend, the reader is referred to the web version of this article.)

due to timing uncertainties. Thus our conclusions mostly rest on results obtained during the period when the gas influx was high and the subsequent longer period during which time the gas efflux was weaker.

4. Air–sea O_2 fluxes from covariance

4.1. Float performance

The next two analyses exploit the Lagrangian nature of the floats. The accuracy of these analyses depends on the accuracy to which the floats are Lagrangian. The following diagnostics suggest that the floats are slightly buoyant, but that this effect is not sufficiently large to produce large biases in turbulent statistics computed from the floats.

The most important factor affecting float performance is its buoyancy, i.e., its residual weight resulting from differencing between its density and that of the surrounding water. Buoyancy affects float performance by causing it to move relative to the surrounding water. Typically, the float's relative motion must be comparable to the rms water velocity for this effect to be large. For a relatively large float buoyancy of 10 g, the relative velocity is estimated as 0.01 m s^{-1} (D'Asaro, 2003a) using a quadratic drag law. This is well below the rms velocities at the height of the storm, 0.1 m s^{-1} rms, and still less than the rms vertical velocity, about 0.02 m s^{-1} rms, at the end of our data. Thus the large water velocities under a hurricane tend to reduce the effects of float buoyancy.

The simplest dynamical diagnostic of float performance is the probability distribution of float depth. If the float is Lagrangian and moving in a layer of turbulent fluid, then because turbulence acts to uniformly mix the layer, the float should spend equal times at each depth in the layer. If, however, the float is light (heavy) relative to the water, it will spend more time at the top (bottom) of the layer. Numerical simulations (Harcourt et al., 2002; D'Asaro et al., 2002) confirm this behavior and show that if the depth distribution of floats is sufficiently nonuniform, the float will not sample the turbulent properties accurately. D'Asaro (2003b) shows that a useful diagnostic of this effect for oceanic mixed layers is the skewness of the depth distribution $S_z=M_3/M_2^{1.5}$, where $M_n=\langle(z-\langle z\rangle)^n\rangle$ is the nth moment of depth z and $\langle\rangle$ is an average over all data. For a neutrally buoyant float S_z is slightly positive; values larger than 1 imply a strongly buoyant float.

Fig. 11 shows the histograms $\Pi(P)$ of float pressure in 0.2-day time bins. Generally, the distributions are nearly uniform down to 20–40 m, the mixing layer depth, often with a slight decrease with increasing depth in the layer. The position of the black circle at 35-m depth plots $S_z/3$ so that the vertical line corresponds to $S_z=0.33$. The mean value of S_z is 0.5, suggesting a slightly buoyant float.

The near-surface bin of the histograms in Fig. 11 is almost always larger than the mean of the next 9 bins (vertical line). This appears to be primarily an effect associated with the finite float size. In the interior of the ocean, the float most closely follows the Lagrangian trajectory running approximately through its center.

However, if this trajectory gets closer than half a float length, $L/2$, to the surface, the float cannot follow, because it cannot get closer than $L/2$ to the surface. Accordingly, the ocean effectively extends a distance $L/2$ above the shallowest depth of the float. At best, the additional time that water spends in this unsampled part of the ocean should be reflected in a larger value for the topmost histogram bin. Physically this would mean that the float was pinned up against the surface as the water that it was following moved above it and then rejoined the water, or similar water, as it moved back down. The histogram depth bins in Fig. 11 have been chosen to have a width of $L=1.4$ m so that the top bin would be 1.5 times higher than its neighbors under these conditions. The grey dots in Fig. 11 show the height of the top histogram bins divided by 1.5, $\Pi(0)/1.5$. The histogram of these values (Fig. 11h) shows them to fall only slightly above 1 on average, indicating that the depth distribution of the floats near the surface is nearly as close to uniform as could be expected from floats of this size. The small difference is again consistent with slightly buoyant floats.

4.2. Gas injection by bubbles

Examination of the O_2 variations along float trajectories provides direct evidence of gas injection at depth (Fig. 12). Five float trajectory segments during the time of maximum gas fluxes are shown. Rapidly descending currents (0.2–0.3 m s^{-1}) carry the floats downward from the wave breaking zone (Fig. 12a,b). Near 10-m depth, the dissolved O_2 (Fig. 12a colors, Fig. 12d, red) and the measured salinity (Fig. 12b, colors) simultaneously increase. The salinity increase is interpreted as a change in conductivity due to the dissolution of bubbles. Salinity is calculated from seawater conductivity and conductivity is reduced if bubbles are present in the conductivity cell. We assumed that observed deviations in conductivity are associated with variations in bubble concentrations (Vagle and Farmer, 1998), rather than salts, to estimate the seawater void-fraction (VF), defined as the volume of air per volume of water (Fig. 12c). The O_2 in these bubbles is estimated using a standard mole fraction for O_2 in dry tropospheric air of 0.20946. Fig. 12d plots the dissolved O_2 (red) relative to values in the interior of the layer and O_2 within bubbles (black). The increases in O_2 at 10–20 m depth are very large, 10 μmol kg^{-1} , and accompanied by a similarly large decrease in estimated bubble gas. These observations suggest that bubbles, generated by breaking waves near the surface, are carried downward by descending currents and dissolve near 10-m depth, thereby injecting air into the water at this depth.

4.3. Covariance O_2 flux

Covariance- or eddy correlation-flux measurements, when properly done, are considered the most reliable estimates of air–sea fluxes because they require the fewest physical assumptions (Fairall et al., 2000). Profiles of the

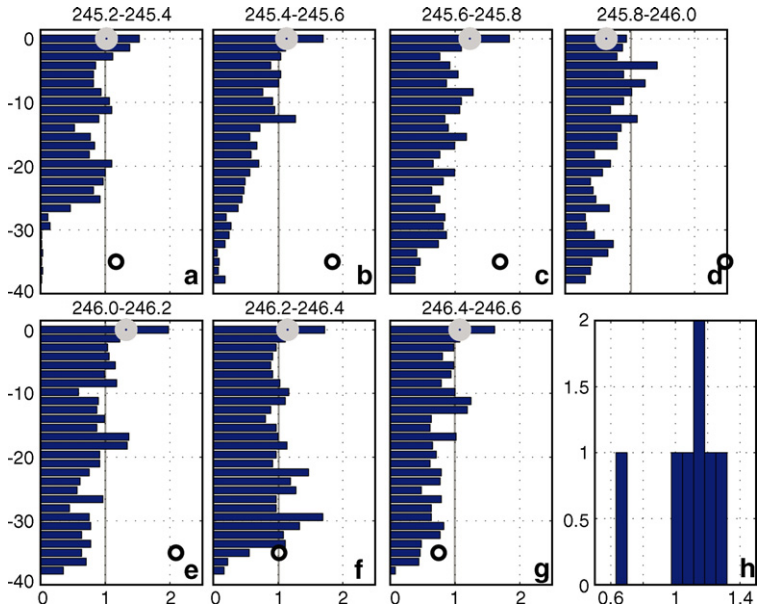

Fig. 11. Float depth distribution. (a–g) Histograms of float depth in 0.2-day time windows normalized so that mean of bins 2–10 equals 1 (grey line). Depth bins are 1.4 m (the float length) deep. Grey circles shown height of first bin/1.5. Black circles show skewness of histogram (×3) so that grey line implies a skewness of 1/3. (h) Histogram of values of gray circle position.

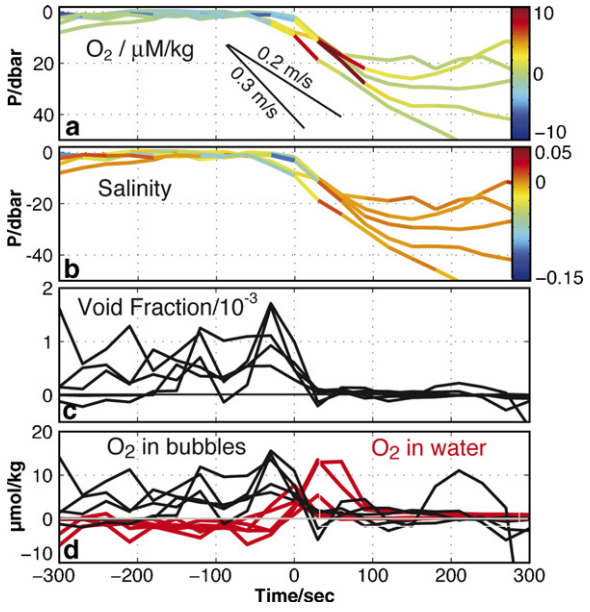

Fig. 12. Evidence for direct injection of O_2 by complete bubble dissolution. (a) Selected trajectories of water-following Langrangian floats as they are swept from near the surface into the ocean interior by currents. Diagonal lines indicate vertical velocities. Trajectory color is O_2. (b) Same but colored by measured salinity anomaly (i.e., approximately the conductivity anomaly) with respect to deeper values. (c) Salinity anomaly interpreted as due to bubbles, so that "fresher," less conductive water has more bubbles. (d) Dissolved O_2 anomaly (red) relative to deep water and O_2 contained in bubbles (black) derived from the salinity anomaly. The simultaneous increase in O_2 and decrease in bubbles suggests bubble dissolution and O_2 injection near 10-m depth. The near-surface region (right) has a surplus of bubble O_2 and a deficit of dissolved O_2 relative to the ocean interior (left). (For interpretation of the references to colour in this figure legend, the reader is referred to the web version of this article.)

average vertical advective eddy flux of oxygen $\langle wO_2' \rangle(z)$ were computed from the float data during the periods of Lagrangian drift and extrapolated to the surface to produce estimates of the surface O_2 exchange rate F_{CO}. These fluxes are shown by the black–yellow circles in Fig. 10a.

The methods follow those developed for heat flux and described in detail by D'Asaro (2003b, 2004). In a horizontally homogeneous turbulent boundary layer, the vertical turbulent transport will control the rate of change of gas concentration via

$$\frac{\partial \langle O_2 \rangle}{\mathrm{d}t} = -\frac{\partial}{\partial z}\langle wO_2' \rangle + S_g \qquad (5)$$

where the $\langle\rangle$ indicates an average at a given depth. The local rate of change of gas (left) depends on the sum of the gradient of turbulent flux (center term) and local sources of gas S_g. Because the layer is well mixed, the first term does not vary with depth. Therefore, in the layer interior where there are no sources of gas, $S_g = 0$, $\langle wO_2' \rangle(z)$ will vary linearly with depth. Near the surface, however, gas is supplied by the atmosphere and all three terms are important. Linearly extrapolating across this near-surface layer using data from the interior yields the surface gas flux F_{CO}. Our sign convection is that fluxes into the ocean are positive.

Although Eq. (5) and the fundamental theoretical approach used to compute the eddy covariance fluxes is standard in laboratory and micro-meteorological studies of boundary layers, the sampling method used here is quite different. Traditionally, a large number of measurements of w and O_2 are made at one distance from the boundary. Here, measurements of O_2 are made along the trajectory of the float and the motion of the float itself defines w. The data are then grouped by distance from the surface and the products wO_2 in each group averaged to make a profile of flux as a function of distance from the surface. Traditionally, statistical convergence is obtained by measuring long enough for many eddies to pass by the sensor. Here, it is obtained by allowing the float to travel around the eddies many times. Traditionally, this requires sensors that have a sufficiently fast response to measure the rapid transit of the eddies past the sensor. Here, the float typically takes many hundreds of seconds to make a complete circuit around the large eddies of the boundary layer. Accordingly, the sampling interval, 30 s, and sensor response time, approximately 8 s for 99% equilibration, are more than adequate. Furthermore, the float measurements of vertical velocity are almost entirely insensitive to surface waves (see Section 2.1.2), so that rapid sampling is not necessary to resolve and remove surface wave noise.

Vertical velocity $w = \frac{DP}{Dt}$ was computed directly from the measured pressure in decibars. The perturbation oxygen concentration O_2' was computed as the difference between the measured concentration and a running time mean of length $T = 2000$ s. Varying T from 1000 s to 16000 s or using other schemes to separate the mean and perturbations does not significantly change the results, although larger values of T increase the noise in the estimate. For a given time interval of data over which a flux was computed, a set of depth bins extending from the surface to the deepest float depth during that interval was defined. The flux in each bin was computed as the average value of wO_2' over all times that the float was in the bin. These data were fit with a line and extrapolated to the surface to yield F_{CO}. Statistical errors in the surface fluxes were estimated from the larger of one standard deviation of bootstrap estimates on the linear fit and half the difference between the estimates from the two different floats. The fluxes, and errors, are plotted as yellow/black circles in Fig. 10a.

The profiles of $\rho\langle wO_2'\rangle$ are shown in Fig. 13 for four time intervals. Fig. 13a shows three profiles taken after the time of maximum flux. The ocean is supersaturated during this time and all three fluxes are out of the ocean. The profiles are roughly linear, as expected, and easily yield a surface flux F_{CO}. These fluxes are probably more accurate than the bulk fluxes during this time.

The covariance flux profile at the time of maximum bulk flux (Fig. 13b) has a peak at about 10-m depth, much deeper than the profiles in Fig. 13a. Furthermore, the profile is only linear below about 12 m. This shape, and the evidence in Fig. 12, suggests a source of dissolved gas near 10 m. More formally, we could define the total O_2 as $O_{2tot}=O_{2bub}+O_2$, i.e., the sum of O_2, the usual dissolved component and O_{2bub}, the O_2 contained in bubbles. In the presence of bubbles, the flux $\rho\langle wO_{2tot}\rangle$, rather than $\rho\langle wO_2'\rangle$, should be linear with depth, as indicated schematically by the magenta curve (Fig. 13b). The bubble flux $\rho\langle wO_{2bub}\rangle$ is the difference between these and is indicated schematically by the cyan curve (Fig. 13b). Unfortunately, conductivity based measurements of O_{2bub}, as in Fig. 12, are not sufficiently accurate to compute the bubble flux directly by covariance. A surface flux of oxygen is found by extrapolating the profile of $\rho\langle wO_{2tot}'\rangle$ (black) to the surface.

The error in the covariance estimate of surface flux at the peak of the storm is large. The large bubble flux region requires extrapolation over a wider region than in Fig. 13a. Furthermore, the averages are dominated by a small number of large events. Thus, for example, the subsurface covariance maximum is about three times larger for float 22 alone than for float 21 alone. The values for float 22 are much larger than the bulk fluxes, suggesting that float 22 may have passed through a region of unusually active bubble injection. The value plotted in Fig. 10 is a subjective average of various estimates. The bulk flux is most likely a more accurate estimate of the true surface flux at this time. Both bulk and covariance methods unambiguously indicate a flux of gas into the ocean.

4.4. Air–sea O_2 flux from surface deficit

At the time of maximum flux (days 245.6–246), dissolved O_2 in the upper few meters is 1–2 μmol kg^{-1} less than within the deeper well-mixed layer (Fig. 14b). The circles plot the deviation of each O_2 measurement from a cubic polynomial fit O_{2M} to all O_2 data between 2.4 and 15 dbar for days 245.6–245.8. Most of the data is tightly clustered around zero, consistent with the layer being well mixed. A few very large positive anomalies correspond to bubble injection. Near the surface, there is a clear negative anomaly. We attribute this to the drawdown of gas concentration as gas fluxes out of the surface due to the oceanic supersaturation. We compute this "surface" flux

$$F_{SO} = \Delta O_2/\tau_\delta \tag{6}$$

from the ratio of the integrated O_2 deficit

$$\Delta O_2 = \int_\delta^0 (O_2 - O_{2M})dz \tag{7}$$

across the surface layer of depth δ and the residence time τ_δ of water in this layer. The value of τ_δ is computed directly from the average time that floats spend above δ. In other words, we expect that the near-surface deficit is being continually mixed with the layer interior as water exchanges between these regions. The deficit can only be maintained against this exchange by a flux out of the ocean. New parcels of water, with gas concentration O_{2M} enter the surface layer from below; gas is flushed out of them, either by exchange across the surface or due to the growth of bubbles, thereby lowering the near-surface gas concentration. The surface flux is estimated from the rate of exchange of gas from below using Eq. (6).

Fig. 14a shows the near-surface region in detail. The small circles show the data, the red line shows this

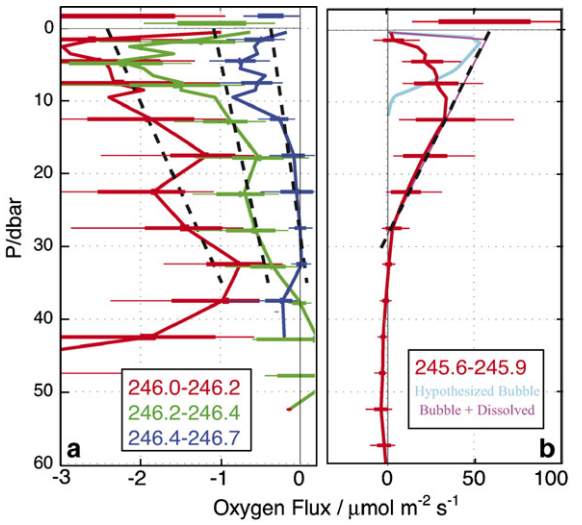

Fig. 13. Estimates of covariance oxygen flux. Profiles of $\langle wO_2'\rangle$ as a function of depth for four time periods. Horizontal lines are 66% and 95% confidence limits based on the bootstrap distribution of all pairs. Dashed line is linear fit. Horizontal bars above 0 dbar are surface flux estimated from extrapolation of line. (a) Post-storm period. Flux is out of the ocean. Line is fit from 10 to 35 m. (b) Time of maximum flux. Flux is into the ocean. Line is fit from 12 to 30 m. Note large-scale change from (a) to (b). Hypothesized bubble (cyan) and resulting total (magenta) O_2 fluxes are shown by dashed lines. (For interpretation of the reference to colour in this figure legend, the reader is referred to the web version of this article.)

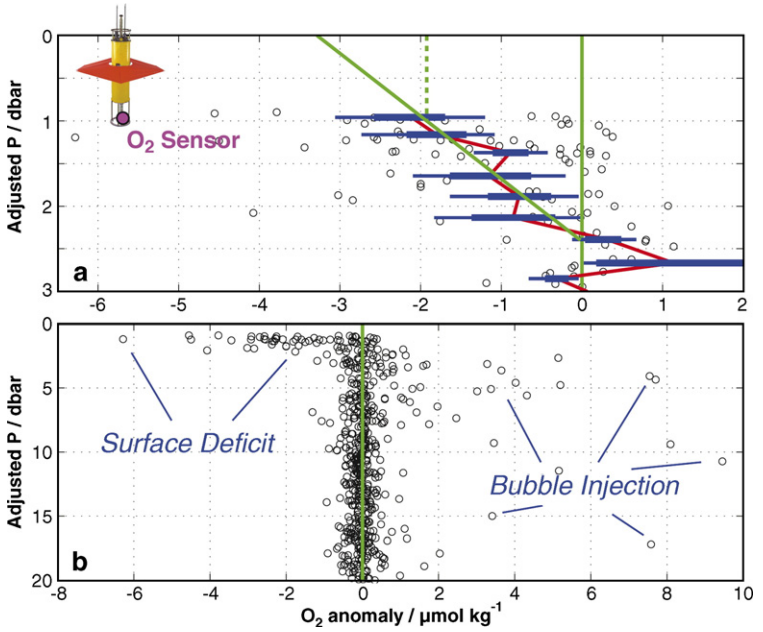

Fig. 14. Near surface O_2 deficit. Measured O_2 (circles) at time of maximum flux (days 245.6–245.8) relative to average value between 1 m and 15 m. (a) Near surface region. (b) To 20 db. Panel (b) shows the low surface O_2 values relative to the interior. Panel (a) shows the data (circles), bin averaged (red) with 95% and 66% confidence limits (blue) and extended to the true surface (green) with two different models. Lagrangian float (a slightly different model than used in this experiment) is shown to scale with location of O_2 sensor intake. Pressure has been adjusted so that the surface is about 1 m above the shallowest float pressure measurement. (For interpretation of the references to colour in this figure legend, the reader is referred to the web version of this article.)

averaged in depth bins with blue confidence limits. The pressure axis has been adjusted so that the shallowest data point is about a float length from the true surface. A picture of the float is shown to scale. Accordingly, the O_2 concentration was not measured and therefore unknown in the upper meter. The solid and dashed green lines show two different extrapolations across the upper meter yielding estimates of ΔO_2 of 3.9 and 3.2 µmol kg^{-1} m, respectively. The residence time τ_δ of floats above δ=2.4 db is 88±28 s, the errors corresponding to 95% bootstrap estimates. The resulting fluxes are 45±16 µmol m^{-2} s^{-1} and 37±13 µmol m^{-2} s^{-1} for the two extrapolation methods, respectively. A similar calculation for the period 245.8–246, with lower wind, shows smaller measured deficits, 0.76 and 0.68 µmol kg^{-1} m, a similar renewal time of 86±20 s and fluxes of 9±2 µmol m^{-2} s^{-1} and 8±2 µmol m^{-2} s^{-1}, respectively.

5. Summary and discussion

5.1. Gas fluxes at hurricane winds

Fig. 15 graphically summarizes the results of the preceding analyses for the hurricane force winds, 30–55 m s^{-1}. Key elements during this time are the following.

5.1.1. A net gas flux into the ocean

The net gas fluxes are into the ocean (positive) even though the water is supersaturated with respect to the local

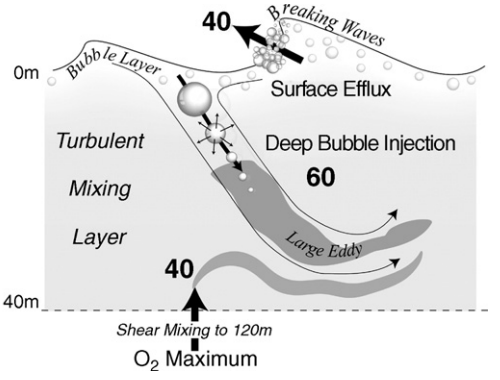

Fig. 15. Cartoon of upper ocean O_2 transfers (µmol m^{-2} s^{-1}) during the hurricane force winds (30–55 m s^{-1}) of Hurricane Frances (days 245.6–245.8). Breaking waves, plotted roughly to scale in the figure, create a near-surface bubble layer. These bubbles are swept downward by the large eddies of the 40-m thick turbulent mixed layer, compress and dissolve at 10–20 m depth, thereby injecting O_2 at about 60 µmol m^{-2} s^{-1}. Intense shear-driven mixing to 120 m brings up O_2 rich water from the subsurface maximum to contribute about 40 µmol m^{-2} s^{-1}. These two fluxes supersaturate the mixed layer by about 5%. A bubble-mediated surface efflux of about 40 µmol m^{-2} s^{-1} partially relieves the supersaturation and results in a near-surface O_2 deficit layer. The net result is to increase the O_2 concentration by about 10 µmol kg^{-1}.

atmospheric pressure by up to 11%. For O_2, this result is obtained by two different methods, eddy covariance (F_{CO}) and a mixed layer budget (F_{BO}). The same result is obtained using a mixed layer budget for N_2 (F_{BN}). Results from two nearby instruments yield consistent results.

5.1.2. Deep bubble injection

The dominant gas-transfer process is the dissolution of air into the water at a depth of approximately 10 m. This occurs via the creation of bubbles by wave breaking and their subsequent transport downward by large eddies of the turbulent boundary layer. Several lines of evidence support this interpretation. First, the net air–sea fluxes are countergradient. Bubble injection, unlike diffusive transport, can affect such fluxes. Second, the ratio of the fluxes of O_2 and N_2, $R_{NO}=F_{BO}/F_{BN}$ (Fig. 10c, Schmidt number scaling, blue shaded region), is consistently below the value implied by Eq. (1). Its value is close to the molar ratio of air (Fig. 10c, green line), consistent with the direct injection of air into the water by dissolving bubbles. Third, variations of O_2 and void fraction, i.e., bubbles, along the trajectories of water parcels descending from the surface show the simultaneous disappearance of bubbles and appearance of a comparable concentration of dissolved O_2 at about 10 m (Fig. 12). Fourth, the profiles of covariance O_2 flux (Fig. 13b) indicate a source of

Table 2
Estimated fluxes and associated data

ID	Start (day)	End (day)	Flux ($\mu M\ m^{-2}\ s^{-1}$)	Error ($\mu M\ m^{-2}\ s^{-1}$)	Wind speed ($m\ s^{-1}$)			T (°C)	Gas ($\mu M\ kg^{-1}$)	Saturation ($\mu M\ kg^{-1}$)
					Center	Start	End			
Covariance fluxes										
1	245.20	245.43	−0.4	0.2	17.9	15.3	22.3	29.1	195.8	190.6
1	245.43	245.65	2.4	1.4	29.9	22.3	42.6	29.0	197.5	189.7
1	245.60	245.90	46.7	30.0	54.9	35.2	37.6	28.1	208.2	188.8
1	245.80	246.00	3.6	4.3	37.6	52.5	31.5	27.4	209.2	193.4
1	246.00	246.20	−2.7	0.6	26.8	31.5	23.3	27.2	208.8	195.9
1	246.20	246.40	−2.2	0.7	20.4	23.3	17.6	27.1	208.5	196.7
1	246.40	246.70	−0.9	0.2	14.4	17.6	12.5	27.0	207.7	197.2
Surface fluxes										
3	245.60	245.80	−37.0	13.0	50.4	35.2	52.5	28.4	205.2	188.2
2	245.60	245.80	−45.0	16.0	50.4	35.2	52.5	28.4	205.2	188.2
3	245.80	246.00	−9.0	2.0	37.6	52.5	31.5	27.4	209.2	193.4
2	245.80	246.00	−8.0	1.5	37.6	52.5	31.5	27.4	209.2	193.4
Bulk fluxes										
5	245.65	245.65	93.7	23.4	42.6	42.6	42.6	28.8	376.1	357.0
4	245.65	245.65	12.4	3.1	42.6	42.6	42.6	28.8	201.1	188.4
5	245.70	245.70	159.0	39.7	50.4	50.4	50.4	28.4	384.8	356.2
4	245.70	245.70	46.1	11.5	50.4	50.4	50.4	28.4	205.2	188.2
5	245.77	245.77	91.6	22.9	54.8	54.8	54.8	27.9	393.6	357.8
4	245.77	245.77	13.6	3.4	54.8	54.8	54.8	27.9	208.8	189.3
7	245.47	245.47	−0.6	0.4	24.9	24.9	24.9	29.1	366.5	360.4
6	245.47	245.47	3.5	2.1	24.9	24.9	24.9	29.1	196.4	190.1
7	245.90	245.90	−17.6	10.5	37.6	37.6	37.6	27.4	395.8	365.2
6	245.90	245.90	−3.3	2.0	37.6	37.6	37.6	27.4	209.2	193.4
7	246.00	246.00	−38.3	23.0	31.5	31.5	31.5	27.3	394.7	368.1
6	246.00	246.00	−7.2	4.3	31.5	31.5	31.5	27.3	209.2	195.0
7	246.10	246.10	−20.9	12.5	26.8	26.8	26.8	27.2	392.9	369.7
6	246.10	246.10	−3.6	2.2	26.8	26.8	26.8	27.2	208.8	195.9
7	246.20	246.20	−11.9	7.1	23.3	23.3	23.3	27.1	392.5	370.7
6	246.20	246.20	−2.1	1.3	23.3	23.3	23.3	27.1	208.6	196.4
7	246.30	246.30	−11.7	7.0	20.4	20.4	20.4	27.1	391.5	371.3
6	246.30	246.30	−4.6	2.8	20.4	20.4	20.4	27.1	208.5	196.7
7	246.40	246.40	−6.8	4.1	17.6	17.6	17.6	27.1	390.8	371.7
6	246.40	246.40	−6.1	3.7	17.6	17.6	17.6	27.1	208.0	196.9
7	246.47	246.47	−8.6	5.1	16.0	16.0	16.0	27.1	390.9	371.9
6	246.47	246.47	−4.3	2.6	16.0	16.0	16.0	27.1	207.8	197.1

ID key: (1) covariance O_2, (2) surface O_2, (3) surface O_2 different extrapolation, (4) bulk O_2 'fast', (5) bulk N_2 'fast', (6) bulk O_2 'slow', (7) bulk N_2 'slow'.

dissolved O_2 at about 10-m depth, requiring a bubble flux of O_2 from the surface to about 10 m.

5.1.3. Entrainment

The strong, rapidly increasing and anti-clockwise rotating winds on the right-hand side of a hurricane are highly effective at mixing the upper ocean both through direct surface forcing and through the generation of near-inertial shear. Because both N_2 and O_2 increase with depth before the storm (Fig. 6), vertical mixing acts to increase the mixed layer concentration of these gases, just as it acts to cool the surface by the upward mixing of colder waters (Section 3). The combination of bubble gas fluxes from above and entrainment gas flux from below causes the mixed layer to become supersaturated in N_2 and O_2.

5.1.4. Surface outgassing

The supersaturation of the ocean drives a flux of gas out of the ocean surface as shown by the reduction in O_2 concentrations in the upper 2 m (Fig. 14, Section 4.4). The magnitude of this O_2 deficit, plus an estimate of the water residence time in this layer, leads to an estimate of the outgassing rate F_{SO}.

5.1.5. Timing relative to the wind

The time of maximum gas fluxes (F_{BN} and F_{BO}) is about 5000 s before the time of maximum winds (Fig. 10a, green line) and nearly simultaneous for both O_2 and N_2. It is tempting to attribute this to increased wave breaking during times of increasing wind speed and growing seas. However, it could also result from temporally unresolved changes in the storm wind field (Section 2.4) associated with an ongoing eyewall replacement cycle.

5.1.6. Overall balance

The bold numbers in Fig. 15 show the approximate magnitude of these processes. Over the top 40 m, roughly the depth of active, large-eddy mixing as measured by the float trajectories, bubble injection is the largest term, with outgassing roughly balancing entrainment. However, over the entire mixed layer, which extends to 120 m (Fig. 2b), the entrainment term dominates.

5.2. Gas fluxes at lower winds

From days 246 to 246.5, the winds decreased from 30 m s^{-1} to 15 m s^{-1}. During this time, the ocean is supersaturated by about 5% and the flux is out of the ocean. The molar gas ratio R_{NO} (Fig. 10c) remains near that of air at all but the lowest wind speeds, although the errors are large. The gas transfer is therefore qualitatively similar to those predicted by Eq. (1). A quantitative discussion of the flux scaling appears in McNeil and D'Asaro (2007-this issue).

5.3. Data compilation

Table 2 lists discrete values of the measured fluxes and their estimated errors. Bulk flux values are taken from the curves in Fig. 3 at intervals of 0.1 day. For each estimate, the estimated saturation gas levels and the range of wind speeds for the interval over which the flux is calculated are also shown.

Acknowledgements

This work was supported by the National Science Foundation and the Office of Naval Research. Measurements were made as part of the CBLAST program. Logistical support and environmental data were provided by supported by NOAA's Hurricane Research Division, especially Peter Black. Air deployments were made by the 53rd Squadron, Air Force Reserve, "Hurricane Hunters." We gratefully acknowledge Thomas Sanford's generous permission to use and publish his EM-APEX data.

References

Bates, N.R., 2002. Interannual variability in the global ocean uptake of CO_2. Geophys. Res. Lett. 29 (5), 1059. doi:10.1029/2001GL013571.

Bates, N.R., Knap, A.H., Michaels, A.F., 1998. Contribution of hurricanes to local and global estimates of air–sea exchanges of CO_2. Nature 395, 58–61.

Black, P.G., D'Asaro, E.A., Drennan, W.M. French, J.R., Niiler, P.P., Sanford, T.B., Terrill, E.J. Walsh, E.J., Zhang, J., in press. Air–sea exchange in hurricanes: synthesis of observations from the coupled boundary layer air–sea transfer experiment. Bull. Am. Met. Soc.

Cione, J.J., Black, P.G., Houston, S.H., 2000. Surface observations in the hurricane environment. Mon. Weather Rev. 128, 1550–1561.

Conkright, M.E., Antonov, J.I., Baranova, O., Boyer, T.B., Garcia, H.E., Gelfeld, R., Johnson, D., Locarnini, R.A., Murphy, P.P., O'Brien, T.D., Smolyar, I., Stephens, C., 2002. World Ocean Database 2001, Volume 1: Introduction. In: Levitus, S. (Ed.), NOAA Atlas. NESDIS, vol. 42. U.S. Government Printing Office, Washington, D.C., pp. 1–167.

D'Asaro, E.A., 2003a. Performance of autonomous Lagrangian floats. J. Atmos. Ocean. Technol. 20, 896–911.

D'Asaro, E.A., 2003b. The ocean boundary layer below Hurricane Dennis. J. Phys. Oceanogr. 33, 561–579.

D'Asaro, E.A., 2004. Air–sea heat flux measurements from nearly neutrally buoyant floats. J. Atmos. Ocean. Technol. 21, 1086–1094.

D'Asaro, E.A., Farmer, D.M., Osse, J.T., Dairiki, G.T., 1996. A Lagrangian float. J. Atmos. Ocean. Tech. 13 (6), 1230–1246.

D'Asaro, E.A, Winters, K.B., Lien, R.C., 2002. Lagrangian analysis of a simulated convective mixed layer. J. Geophys. Res. 107. doi:10.1029/2000JC000247.

Farmer, D.M., McNeil, C.L., Johnson, B.D., 1993. Enhanced air–sea gas flux due to bubbles. Nature 361, 620–623.

Fairall, C.W., Hare, J.E., Edson, J.B., McGillis, W., 2000. Parameterization and micrometeorological measurement of air–sea gas transfer. Boundary - Layer Meteorol. 96, 63–105.

Garcia, H.E., Gordon, L.I., 1992. Oxygen solubility in seawater: better fitting equations. Limnol. Oceanogr. 37, 1307–1312.

Hamme, R.C., Emerson, S.R., 2004. The solubility of neon, nitrogen and argon in distilled water and seawater. Deep-Sea Res. I 51 (11), 1517−1528.

Harcourt, R.R., Steffen, E.L., Garwood, R.W., D'Asaro, E.A., 2002. Fully Lagrangian floats in Labrador Sea deep convection: comparison of numerical and experimental results. J. Phys. Oceanogr. 32, 493–510.

Keeling, R.F., 1993. On the role of large bubbles in air–sea gas exchange and supersaturation in the ocean. J. Mar. Res. 51 (2), 237–271.

Liss, P.S., Merlivat, L., 1986. Air–sea gas exchange rates: introduction and synthesis. In: Buat-Menard, P. (Ed.), The Role of Air–Sea Exchange in Geochemical Cycling. Reidel, Dordrecht, pp. 113–127.

Liss, P.S., Slater, P.G., 1974. Flux of gases across the air–sea interface. Nature 247, 181–184.

McNeil, C.L., D'Asaro, E.A., 2007. Parameterization of air–sea gas exchange at extreme winds. J. Mar. Sys. 66, 110–121 (this issue). doi:10.1016/j.jmarsys.2006.05.013.

McNeil, C.L., D'Asaro, E.A., Johnson, B.D., Horn, M., in press. A gas tension device with response times of minutes. J. Atmos. Ocean. Tech. doi:10.1175/JTECH1974.1.

McNeil, C.L., Katz, D.R., Wanninkhof, R., Johnson, B.D., 2006. Continuous shipboard sampling of dissolved N_2, O_2 and CO_2. Deep-Sea Res. I 52, 1767–1785.

Nightingale, P.D., Malin, G., Law, C.S., Watson, A.J., Liss, P.S., Liddicoat, M.I., Boutin, J., Upstill-Goddard, R.C., 2000. In situ evaluation of air–sea gas exchange parameterization using novel conservative and volatile tracers. Glob. Biogeochem. Cycles 14, 373.

Powell, M.D., Houston, S.H, Amat Jr., L.R., Morisseau-Leroy, N., 1998. The HRD real-time hurricane wind analysis system. J. Wind Eng. Ind. Aerodyn. 77–78, 53–64.

Uhlhorn, E.W., Black, P.G., 2003. Verification of remotely sensed sea surface winds in hurricanes. J. Atmos. Ocean. Technol. 20, 99–116.

Vagle, S., Farmer, D.M., 1998. A comparison of four methods of bubble measurement. IEEE J. Oceanic Eng. 23, 211–222.

Wanninkhof, R., 1992. Relationship between wind speed and gas exchange over the ocean. J. Geophys. Res. 97 (C5), 7373–7382.

Wannikhof, R., McGillis, W.R., 1999. A cubic relationship between air–sea CO_2 exchange and windspeed. Geophys. Res. Lett. 26, 1889–1892.

Watson, A.J., Upstill-Goddard, R.C., Liss, P.S., 1991. Air–sea gas exchange in rough and stormy seas measured by a dual-tracer technique. Nature 349, 145–147.

Woolf, D.K., 1997. Bubbles and their role in gas exchange. In: Liss, P.S., Duce, R.A. (Eds.), The Sea Surface and Global Change. Cambridge University Press, Cambridge, pp. 173–205.

Woolf, D.K., Thorpe, S.A., 1991. Bubbles and the air–sea exchange of gases in near-saturation conditions. J. Mar. Res. 49, 435–466.